Revision 2

Word count: 5951

Iron and aluminum substitution mechanism in perovskite phase in the system $MgSiO_3$-$FeAlO_3$-MgO

Takayuki Ishii*[,1,2], Catherine McCammon[2], Tomoo Katsura[2]

Affiliations:

[1]Center for High Pressure Science and Technology Advanced Research, Beijing, 100094, China

[2]Bayerisches Geoinstitut, University of Bayreuth, Universitätsstraße 30, 95447 Bayreuth, Germany

***Corresponding author:** Takayuki Ishii (takayuki.ishii@hpstar.ac.cn)

Abstract

Fe,Al-bearing $MgSiO_3$ perovskite (bridgmanite) is considered to be the most abundant mineral in Earth's lower mantle, hosting ferric iron in its structure as charge-coupled (Fe_2O_3 and $FeAlO_3$) and vacancy components ($MgFeO_{2.5}$ and $Fe_{2/3}SiO_3$). We examined concentrations of ferric iron and aluminum in the perovskite phase as a function of temperature (1700-2300 K) in the $MgSiO_3$-$FeAlO_3$-MgO system at 27 GPa using a multi-anvil high-pressure apparatus. We found a $LiNbO_3$-structured phase in the quenched run product, which was the perovskite phase under high pressures and high temperatures. The perovskite phase coexists with corundum and a phase with $(Mg,Fe^{3+},□)(Al,Fe^{3+})_2O_4$ composition (□: vacancy). The $FeAlO_3$ component in the perovskite phase decreases from 69 to 65 mol% with increasing temperature. The Fe_2O_3 component in the perovskite phase remains at ~1 mol% constant with temperature.

The A-site vacancy component of $Fe_{2/3}SiO_3$ in the perovskite phase exists as 1-2 mol% at 1700-2000 K, whereas 1 mol% of the oxygen vacancy component of $MgFeO_{2.5}$ appears at higher temperatures, although the analytical errors prevent definite conclusions. The A-site vacancy component might be more important than the oxygen vacancy component for the defect chemistry of bridgmanite in slabs and for average mantle conditions when the $FeAlO_3$ charge-coupled component is dominant.

Keywords: bridgmanite, phase transition, multi-anvil press, high pressure, substitution mechanism, lower mantle

Introduction

$MgSiO_3$ perovskite (bridgmanite) is the most abundant phase in Earth's lower mantle, and incorporates Al and Fe by substituting for Si and Mg. The flexible substitution in bridgmanite produces a wide range of compositional variations depending on pressure-temperature-composition conditions. Although the oxidation state in the lower mantle is considered to be below the iron-wüstite buffer (Frost and McCammon 2008), large amounts of ferric iron are expected in bridgmanite due to charge disproportionation of iron ($3\ FeO \rightarrow Fe_2O_3 + Fe$) when aluminum is present (Lauterbach et al. 2000; Frost et al. 2004; Irifune et al. 2010; Huang et al. 2021).

McCammon et al. (1997) reported an increased ferric iron content with increasing Al in pyroxene diamond inclusions with composition $(Mg,Fe,Al)(Si,Al)O_3$, considered to be derived from bridgmanite. Lauterbach et al. (2000) experimentally also found a positive correlation between Fe^{3+} and Al. These studies suggest that iron favors the ferric state in bridgmanite by mainly forming the $FeAlO_3$ charge-coupled component, making it a major component in bridgmanite.

The $FeAlO_3$ component can significantly affect the properties of bridgmanite. For example, incorporating $FeAlO_3$ decreases the bulk modulus and increases the density (e.g., Boffa Ballaran et al. 2012) and electrical conductivity (e.g., Yoshino et al. 2016). The $FeAlO_3$ component also affects Mg-Fe partitioning between bridgmanite and other lower-mantle ferromagnesian minerals in peridotite and basalt (e.g., Frost and Langenhorst 2002; Irifune et al. 2010). Thus, understanding the $FeAlO_3$ component in bridgmanite is essential to argue the structure and dynamics of the lower mantle.

There are other minor components in bridgmanite. Experiments in the ternary systems of $MgO\text{-}SiO_2\text{-}Al_2O_3$ and $MgO\text{-}SiO_2\text{-}Fe_2O_3$ demonstrated that the oxygen vacancy components such as $MgAlO_{2.5}$ and $MgFeO_{2.5}$ are included in bridgmanite (Navrotsky et al. 2003; Kojitani

et al. 2007; Liu et al. 2017a; Fei et al. 2020; Ishii et al. 2022a). Oxygen vacancy-bearing bridgmanite should be more compressible than stoichiometric bridgmanite. In addition, an A-site vacancy component of $Fe^{3+}_{2/3}SiO_3$ has also been suggested, which should also be compressible (Ismailova et al. 2016). The charge-coupled substitution components Al_2O_3 and Fe_2O_3 can also appear (Kubo and Akaogi, 2000; Kojitani et al. 2007; Liu et al. 2017b; Fei et al. 2020). Although the Al and Fe^{3+} substitution mechanisms have been thus individually investigated in Fe- and Al-free systems, respectively, the substitution mechanisms of these components are still unclear in the Fe-, Al-bearing system.

Liu et al. (2020) investigated chemistry of the perovskite phase in the $MgSiO_3$-$FeSiO_3$-Fe_2O_3-Al_2O_3 system at 27 GPa and 2000 K. They observed 65 mol% of $FeAlO_3$ with a few percent of the oxygen vacancy and A-site vacancy components of $MgFeO_{2.5}$ and $Fe_{2/3}SiO_3$, respectively, using samples with ferrous iron up to 25%. However, the temperature and pressure dependence of chemistry of the perovskite phase in these systems is still unknown.

This study investigated the temperature dependence on chemistry of the perovskite phase in the ferrous iron-free system MgO-$MgSiO_3$-$FeAlO_3$ at 27 GPa and 1700-2300 K using a multi-anvil apparatus. Excess MgO was added to explore the substitution mechanism in mantle assemblages with Mg/Si>1, such as peridotite.

Experimental procedures

Starting material and high-pressure experiments

A mixture of $MgSiO_3$ enstatite, Mg_2SiO_4 forsterite, Al_2O_3 corundum, and Fe_2O_3 hematite with mole proportions of 5:20:37.5:37.5, respectively, was used as a starting material. By following Ishii et al. (2018a; 2019a), the enstatite and forsterite samples were synthesized by dissolving Mg metal in a solution of HNO_3 plus pure water, mixing it with

tetraethylorthosilicate [$(CH_3CH_2O)_4Si$] at Mg/Si ratios of 1 and 2 for enstatite and forsterite, respectively, adding ammonia to the solutions, and heating the resulting gels stepwise to 1700 K. Regent grades of Al_2O_3 and Fe_2O_3 were dried at 773 K for 24 h before weighing.

High pressure-high temperature syntheses were performed at 27 GPa and 1700, 2000, and 2300 K for 2-20 h using IRIS-15, a 15-MN Kawai-type multi-anvil press with an Osugi-type guide block system installed at the Bayerisches Geoinstitut, University of Bayreuth (Ishii et al. 2016; 2019b). The starting material was packed in a Pt-tube capsule, closed with two Pt lids. In order to avoid reduction of Fe^{3+} to Fe^{2+}, which was observed in Liu et al. (2020), an IrO_2 oxidizer was also put at the bottom of the capsule, separating it from the sample using a Pt foil. A Cr-doped MgO octahedron with 7 mm edge lengths was used as a pressure medium. A cylindrical $LaCrO_3$ heater was inserted into the center of the octahedron. An MgO sleeve was placed in the heater to insulate the sample capsule from the heater electrically. Sample temperatures were measured at the surface of the capsule using a W97%Re3%–W75%Re25% thermocouple. The ceramic parts of the cell assemblies were kept at 1273 K for more than 3 h in an oven and taken out just before assembling them. The sample was always kept at 427 K in an oven and taken out just before assembling. The truncation size of the inner anvils was 3.0 mm. The sample was first compressed to 2 GPa (0.3 MN) at room temperature and heated to 600 K at a rate of 100 °C/min. These conditions were kept for 1~2 h to purge adhesive water in the sample and cell components. The assembly was then cooled to room temperature, compressed to 27 GPa (13 MN), and heated to the desired temperature at a rate of 100 °C/min. After keeping the target temperature, the sample was quenched by shutting off the electric power supply of the heater and slowly decompressed for 12-15 h.

To estimate a generated pressure of 27 GPa at 13 MN, we employed a pressure dependence of the alumina content in $MgSiO_3$ bridgmanite coexisting with corundum together with the decomposition pressure of pyrope to bridgmanite plus corundum (Hirose et al. 2001;

Liu et al. 2017b) in separate runs. Pressure calibration has been generally performed using phase boundaries of compounds determined by in-situ X-ray diffraction in a multi-anvil press. However, there is no such pressure calibrant to cover the present pressure range (>27 GPa) (Ito, 2015). Hirose and Fei (2002) calibrated pressures to 27 GPa using Al_2O_3 content in bridgmanite reported by Hirose et al. (2001). Liu et al. (2017b) extended the pressure range to 52 GPa with more systematic data, and therefore the present calibration to estimate 27 GPa is most reliable for the time being. Our recent study reproduced 27.1(5) GPa at 13 MN using the same calibrant in the same multi-anvil press (Ishii et al. 2022b), supporting validity of the present way.

Sample characterization

Phases in the recovered samples were identified using a micro-focused X-ray diffractometer (Bruker, D8 DISCOVER) operated at 40 kV and 500 μA equipped with a two-dimensional solid-state detector (VÅNTEC500) and a micro-focus source (IμS) of Co-Kα radiation. Phase compositions were measured using an electron microprobe analyzer (EPMA) with wavelength-dispersive spectrometers (JEOL, JXA-8200), operated at an accelerating voltage and probe current of 15 kV and 15 nA, respectively. The standards for Mg and Si, Al, and Fe were natural enstatite, synthetic corundum, and synthetic hematite, respectively. Sample textures were observed using a field-emission-type scanning electron microscope (SEM) (Zeiss LEO 1530 Gemini) with a detector for back-scattered electron (BSE) imaging and an energy dispersive X-ray spectrometer (Oxford X-Max^N).

Iron valence ratios in the recovered samples were determined by Mössbauer spectroscopy. The recovered samples were polished to 150 μm thickness. Mössbauer spectra were obtained at room temperature (293 K) in transmission mode on a constant acceleration Mössbauer spectrometer with a nominal 370 MBq ^{57}Co high specific activity source in a 12-μm-thick Rh matrix (McCammon et al. 1991; McCammon 1994). The velocities in all spectra

were calibrated using a reference spectrum of a 25-μm-thick α-Fe foil certified by National Bureau of Standards (now referred to as the National Institute of Standards and Technology, standard reference material no. 1541) at room temperature. Spectra were collected for 1–2 days and fitted with the full transmission integral using MossA software (Prescher et al. 2012).

Results and Discussion

Tables 1 and 2 summarize experimental conditions, phases present, and chemical compositions of each sample. Figure 1 illustrates the room-temperature Mössbauer spectrum of the sample synthesized at 27 GPa and 2000 K. The hyperfine parameters for Mössbauer spectra of the bulk recovered samples obtained by fitting are also summarized in Table 1. Figures 2 and 3, respectively, show a representative X-ray diffraction (XRD) pattern and back-scattered electron (BSE) images of the recovered samples. We applied heating durations of 2-20 h at 1700-2300 K, in which the sample annealed at 2300 K employed only 2 h (Table 1). Many phase-relation studies investigating multi-component systems like pyrolite and basaltic crust compositions by multi-anvil press showed chemically homogeneous phases at 2000-2300 K even by heating for 2 h or less (Ono et al. 2001; Hirose and Fei, 2002; Ishii et al. 2011; 2012; 2018b; 2019c; 2022b). In fact, the well-crystallized texture and the homogeneous chemical compositions of the recovered phases (Tables 1 and 2 and Fig. 3) suggest reaching equilibrium in the present heating durations at the pressure-temperature conditions.

Ferric iron contents

Mössbauer spectra of the bulk recovered samples can be fitted to one doublet, although one broad peak was also detected only on sample I-969 (Fig. 1). The hyperfine parameters of the center shift and quadrupole splitting are 0.32-0.33 mm/s and 0.90-0.93 mm/s, respectively, which are in good agreement with those of Fe^{3+} in bridgmanite and the $LiNbO_3$-structured

158 phases (Fei et al. 1994; McCammon et al. 2004; Hummer and Fei 2012; Liu et al. 2020; Huang
159 et al. 2021). The broad peak of sample I-969 can be assigned to a weakly magnetic Fe^{3+}
160 component. All observed peaks were thus assigned to Fe^{3+}, showing $Fe^{3+}/\Sigma Fe = 100\%$ in all
161 samples.

162

163 *Phase identification*

164 Most XRD peaks were assigned to a $LiNbO_3$-structured phase (Fig. 2), known as a
165 back-transformed phase from a perovskite phase (Leinenweber et al. 1991; Akaogi et al. 2016;
166 Ishii et al. 2017a; Liu et al. 2020). Liu et al. (2020) reported that the $MgSiO_3$-bearing perovskite
167 phase with more than 40% of $FeAlO_3$ was recovered as a lithium-niobate phase at ambient
168 conditions. Therefore, the chemistry of the $LiNbO_3$-structured phase should represent that of
169 the perovskite-structured phase under high pressure-temperature conditions. Hereafter, we
170 refer to this phase as the perovskite phase when discussing the crystal chemistry at high
171 pressure and high temperature.

172 The BSE images showed three phases with different textures and contrasts in addition
173 to the $LiNbO_3$-structured phase. One is a Mg,Al,Fe-rich phase with grain-crack texture. Its
174 main components are $MgAl_2O_4$ and $MgFe_2O_4$, implying that this phase may be one of the
175 $A^{2+}B^{3+}{}_2O_4$ orthorhombic phases, so-called post-spinel (PS) phases, which have an octahedral
176 framework and a trigonal prism site (Ishii et al. 2018c). These phases are difficult to identify
177 because they have similar crystal structures but different atomic distributions (Ishii et al. 2020).
178 The XRD peaks not belonging to the $LiNbO_3$-structured phase can be assigned to a PS phase
179 (Fig. 2). However, the XRD patterns did not clearly indicate which PS phase is due to the few
180 observed peaks. Nevertheless, it can be assigned to the $CaTi_2O_4$-type phase, which was recently
181 discovered in various AB_2O_4 compositions (Funamori et al. 1998; Bindi et al. 2014; Ishii et al.
182 2014; 2015; 2021). We refer to this phase as a PS phase hereafter. The BSE images also indicate

This is the peer-reviewed, final accepted version for American Mineralogist, published by the Mineralogical Society of America.
The published version is subject to change. Cite as Authors (Year) Title. American Mineralogist, in press.
DOI: https://doi.org/10.2138/am-2022-8457. http://www.minsocam.org/

183 limited amounts (~1.5-3 vol.%) of an Al-rich phase, which was identified as corundum because
184 this phase can be regarded as an Al_2O_3-$MgSiO_3$-Fe_2O_3 solid solution. However, XRD patterns
185 indicated no corundum peaks, probably due to the limited intensities. The detailed
186 compositions of these phases are discussed below.

187

188 *Compositions of the perovskite phase*

189 The component fractions in the $ABO_{3\pm\delta}$ perovskite phase were estimated using EPMA and
190 Mössbauer data based on the following assumptions: (1) Al and Fe^{3+} produce the most charge-
191 coupled component of $FeAlO_3$. The remaining trivalent cations are referred to as *T*. (2) When
192 the cation-oxygen ratio is smaller than 2:3, the *A*-site cation-vacancy component $T_{2/3}SiO_3$ is
193 considered. When greater, the oxygen vacancy component $MgTO_{2.5}$ is considered. (3) The
194 remaining *T* produces the charge-coupled component TTO_3. (4) The remaining Mg^{2+} and Si^{4+}
195 produce the $MgSiO_3$ component.

196 Figure 4 shows the changes in components of the perovskite phase with temperature
197 obtained by the above procedure. Fe^{3+} and Al^{3+} ions dominate, resulting in the dominant
198 component $FeAlO_3$. This component slightly decreases with increasing temperature from 69
199 mol% to 65 mol%. The second major component is $MgSiO_3$, which increases with increasing
200 temperature from 28 mol% to 32 mol%. Thus, the perovskite phase in the present system can
201 be approximated by a $MgSiO_3$-$FeAlO_3$ solid solution. Liu et al. (2020) reported that the
202 perovskite phase synthesized at 27 GPa and 2000 K in the $MgSiO_3$-$FeSiO_3$-Fe_2O_3-Al_2O_3
203 system without excess MgO has 63-65 mol% of the $FeAlO_3$ component. These values are
204 slightly smaller than the present study (67 mol% at 2000 K), probably because Fe^{3+} in their
205 perovskite phase (11-15%) was slightly reduced to Fe^{2+} to form some $Fe^{2+}SiO_3$ components.
206 We observed 1~2 mol% of the *A*-site vacancy component of $Fe^{3+}{}_{2/3}SiO_3$ at lower temperatures
207 of 1700 and 2000 K, whereas 1 mol% of the oxygen vacancy component $MgFeO_{2.5}$ was found

208 at 2300 K. Although this change is within the analytical errors, the dominant vacancy
209 component might change with temperature. In addition, we observed small amounts, only 1
210 mol%, of the charge-coupled component Fe_2O_3 in all perovskite phases, which showed no
211 temperature dependence.

212

213 *Compositions of the associated phases*

214 As mentioned above, we found two phases associated with the $LiNbO_3$-structured phase,
215 *i.e.*, the PS phase and corundum. The primary composition of the PS phase can be expressed
216 as $MgAl_2O_4$-$MgFe_2O_4$. However, there are extra ferric irons. Such extra Fe^{3+} should produce
217 an A-site vacancy component $Fe_{2/3}Fe_2O_4$ because the total cation number is less than 3 for 4
218 oxygens. This component is the third most abundant, representing 5-13 mol% of the phase.
219 This phase also has a minor component of Mg_2SiO_4 (2-5 mol%) because of the small amounts
220 of SiO_2 (0.8-1.6 wt.%). The limited Si contents are typical in PS-related oxides, supporting the
221 phase identification as a PS phase (Ishii et al. 2017b; 2018d; Akaogi et al. 2018; Uenver-Thiele
222 et al. 2018). Thus, the compositions of the PS phase can be expressed as $(Mg,Fe^{3+},□)(Al,Fe)_2O_4$.
223 (□: vacancy), and is almost independent of the temperature.

224 The composition of corundum is expressed as Al_2O_3-$MgSiO_3$-Fe_2O_3, as mentioned
225 above. There appears to be almost no temperature dependence, although composition at 1700
226 K is unknown due to the exceedingly small grain sizes (≤~1 μm) for EPMA analysis. The Al_2O_3,
227 $MgSiO_3$ and Fe_2O_3 contents are 80, 10, and 10 mol%, respectively.

228

229 *Reaction controlling the chemistry of the perovskite phase*

230 The present system essentially has four chemical components: MgO, Fe_2O_3, Al_2O_3, and
231 SiO_2. On the other hand, the number of phases is three: perovskite phase, an $A^{2+}B^{3+}{}_2O_4$ PS

phase, and corundum. Therefore, the present system has one degree of freedom at a given pressure and temperature, which would be the partitioning of the $FeAlO_3$ charge-coupled component because Al_2O_3 and Fe_2O_3 are strongly coupled in the perovskite phase in the present system.

The resulting equilibrium reaction may be:

$$\underset{\text{Perovskite phase}}{FeAlO_3} + \underset{PS}{Mg_2SiO_4} = \underset{PS}{MgFeAlO_4} + \underset{\text{Perovskite phase}}{MgSiO_3} \quad (1)$$

The coincident decrease and increase in $FeAlO_3$ and $MgSiO_3$ components, respectively, with temperature (Fig. 4) suggest that the entropy change with this reaction is slightly positive.

Implications

The oxygen-vacancy components $MgAlO_{2.5}$ and $MgFeO_{2.5}$ have been proposed to exist in bridgmanite in the systems MgO-SiO_2-Al_2O_3 and MgO-SiO_2-Fe_2O_3, respectively (Liu et al. 2017a; Fei et al. 2020). The oxygen vacancy components should increase compressibility. Also, they possibly reduce the creep strength of bridgmanite, suggesting a viscosity contrast compared with the mantle containing stoichiometric bridgmanite (Liu et al. 2017a; Reali et al. 2019). The present study demonstrates that the vacancy component changes from A-site cation vacancy to oxygen vacancy with increasing temperature. Thus, the oxygen vacancy components are expected to be present in high-temperature regions such as plumes (White and Mackenzie 1995). On the other hand, the present results suggest that the A-site cation vacancy should be more stable in relatively low-temperature regions such as subducted slabs.

These vacancy components should dominate in shallower regions of the lower mantle, namely the mid-mantle, due to their low density (Liu et al. 2017a). Although the proportions of vacancy components are small, percent-order vacancies should be enough to soften mineral strength (Reali et al. 2019). Therefore, the vacancy components would soften the mid-mantle

to enhance mantle dynamics and geochemical circulation. Slab penetration and stagnation in the mid-mantle (Fukao and Obayashi 2013) and plumes becoming invisible by seismic tomography (French and Romanovicz 2015) may reflect the lower viscosity of the mid-mantle compared to deeper regions.

Vacancy in bridgmanite may also play an important role in incorporating water as OH groups in its crystal structure, which has significant importance for the geochemical evolution of the mantle. The oxygen vacancy component of $MgAlO_{2.5}$ may accommodate water based on the following reaction: $MgAlO_{2.5} + 1/2H_2O \rightarrow MgAlHO_3$ (e.g., Navrotsky, 1999). The oxygen vacancy component of $MgFe^{3+}O_{2.5}$ would also allow incorporation of water in the same manner. The A-site vacancy component of $Fe^{3+}{}_{2/3}SiO_3$ might also have the capability to include water based on the following reaction: $Fe^{3+}{}_{2/3}SiO_3 + 1/3H_2O \rightarrow Fe^{3+}{}_{2/3}(OH)_{1/3}SiO_3H_{1/3}$. Thus, both the vacancy components may be potential hosts for water in the lower mantle.

The pressure dependence of the vacancy components has not been investigated, however. Such a study requires a wide pressure range, which is impossible using conventional multi-anvil technology. On the other hand, no percent-order vacancy components can be detected by diamond anvil experiments due to relatively large chemical heterogeneity. Therefore, future experiments will focus on exploring the pressure dependence of vacancy concentrations to provide better constraints on their influence on lower mantle dynamics. Our ultrahigh-pressure multi-anvil technology (Ishii et al. 2016; 2017c; 2019b; 2022b) provides the best possibility to investigate the pressure dependence, and we will tackle this task in the next study.

References

Akaogi, M., Abe, K., Yusa, H., Ishii, T., Tajima, T., Kojitani, H., Mori, D., and Inaguma, Y. (2017). High-pressure high-temperature phase relations in $FeTiO_3$ up to 35 GPa and 1600 C. Physics and Chemistry of Minerals, 44(1), 63-73.

Akaogi, M., Kawahara, A., Kojitani, H., Yoshida, K., Anegawa, Y., and Ishii, T. (2018). High-pressure phase transitions in $MgCr_2O_4 \cdot Mg_2SiO_4$ composition: Reactions between olivine and chromite with implications for ultrahigh-pressure chromitites. American Mineralogist: Journal of Earth and Planetary Materials, *103*(1), 161-170.

Ballaran, T. B., Kurnosov, A., Glazyrin, K., Frost, D. J., Merlini, M., Hanfland, M., & Caracas, R. (2012). Effect of chemistry on the compressibility of silicate perovskite in the lower mantle. Earth and Planetary Science Letters, 333, 181-190.

Bindi, L., Sirotkina, E., Bobrov, A. V., & Irifune, T. (2014). X-ray single-crystal structural characterization of $MgCr_2O_4$, a post-spinel phase synthesized at 23 GPa and 1600° C. Journal of Physics and Chemistry of Solids, 75(5), 638-641.

Fei, Y., Virgo, D., Mysen, B. O., Wang, Y., & Mao, H. K. (1994). Temperature-dependent electron delocalization in (Mg, Fe)SiO_3 perovskite. American Mineralogist, 79, 826-837.

Fei, H., Liu, Z., McCammon, C., and Katsura, T. (2020). Oxygen vacancy substitution linked to ferric iron in bridgmanite at 27 GPa. Geophysical Research Letters, 47(6), e2019GL086296.

Frost, D. J., and Langenhorst, F. (2002). The effect of Al_2O_3 on Fe–Mg partitioning between magnesiowüstite and magnesium silicate perovskite. Earth and Planetary Science Letters, 199(1-2), 227-241.

French, S. W., and Romanowicz, B. (2015). Broad plumes rooted at the base of the Earth's mantle beneath major hotspots. Nature, 525(7567), 95-99.

Frost, D. J., Liebske, C., Langenhorst, F., McCammon, C. A., Trønnes, R. G., and Rubie, D. C. (2004). Experimental evidence for the existence of iron-rich metal in the Earth's lower mantle. Nature, 428(6981), 409-412.

Frost, D.J., and McCammon, C.A. (2008). The redox state of Earth's mantle. Annual Review of Earth and Planetary Sciences, 36, 389-420

Fukao, Y., and Obayashi, M. (2013). Subducted slabs stagnant above, penetrating through, and trapped below the 660 km discontinuity. Journal of Geophysical Research: Solid Earth, 118(11), 5920-5938.

Funamori, N., Jeanloz, R., Nguyen, J.H., Kavner, A., Caldwell, W.A., Fujino, K., Miyajima, N., Shinmei, T., and Tomioka, N. (1998). High-pressure transformations in $MgAl_2O_4$. Journal of Geophysical Research: Solid Earth, 103(B9), 20813-20818.

Hirose, K., Fei, Y., Ono, S., Yagi, T., and Funakoshi K. (2001) In situ measurements of the phase transition boundary in $Mg_3Al_2Si_3O_{12}$: Implications for the nature of the seismic discontinuities in the Earth's mantle. Earth and Planetary Science Letteers, 184, 567–573.

Hirose, K., and Fei, Y. (2002) Subsolidus and melting phase relations of basaltic composition in the uppermostlower mantle. Geochimica et Cosmochimica Acta, 66, 2099-2108.

Huang, R., Ballaran, T. B., McCammon, C. A., Miyajima, N., Dolejš, D., and Frost, D. J. (2021). The composition and redox state of bridgmanite in the lower mantle as a function of oxygen fugacity. Geochimica et Cosmochimica Acta, 303, 110-136.

Hummer, D. R., and Fei, Y. (2012). Synthesis and crystal chemistry of Fe^{3+}-bearing (Mg, Fe^{3+})(Si, Fe^{3+}) O_3 perovskite. American Mineralogist, 97, 1915-1921.

Irifune, T., Shinmei, T., McCammon, C. A., Miyajima, N., Rubie, D. C., and Frost, D. J. (2010). Iron partitioning and density changes of pyrolite in Earth's lower mantle. Science, 327(5962), 193-195.

Ishii, T., Kojitani, H., and Akaogi, M. (2011). Post-spinel transitions in pyrolite and Mg_2SiO_4 and akimotoite–perovskite transition in $MgSiO_3$: precise comparison by high-pressure high-temperature experiments with multi-sample cell technique. Earth and Planetary Science Letters, 309, 185-197.

Ishii, T., Kojitani, H., and Akaogi, M. (2012). High-pressure phase transitions and subduction behavior of continental crust at pressure–temperature conditions up to the upper part of the lower mantle. Earth and Planetary Science Letters, 357, 31-41.

Ishii, T., Kojitani, H., Tsukamoto, S., Fujino, K., Mori, D., Inaguma, Y., Tsujino, N., Yoshino, T., Yamazaki, D., Higo, Y., Funakoshi, K., Akaogi, M. (2014). High-pressure phase transitions in $FeCr_2O_4$ and structure analysis of new post-spinel $FeCr_2O_4$ and $Fe_2Cr_2O_5$ phases with meteoritical and petrological implications. American Mineralogist, 99, 1788-1797.

Ishii, T., Fujino, K., Kojitani, H., Yusa, H., Mori, D., Inaguma, Y., Matsushita, Y., Yamaura, K. Akaogi, M. (2015). High-pressure high-temperature transitions in $MgCr_2O_4$ and crystal structures of new post-spinel $MgCr_2O_4$ and $Mg_2Cr_2O_5$ phases. American Mineralogist, 100, 59-65.

Ishii, T., Shi, L., Huang, R., Tsujino, N., Druzhbin, D., Myhill, R., Li, Y., Lin, W., Yamamoto, T., Miyajima, N., Kawazoe, T., Nishiyama, N., Higo, Y., Tange, Y., and Katsura, T. (2016). Generation of pressures over 40 GPa using Kawai-type multi-anvil press with tungsten carbide anvils. Review of Scientific Instruments, 87(2), 024501.

Ishii, T., Sinmyo, R., Komabayashi, T., Ballaran, T. B., Kawazoe, T., Miyajima, N., Hirose, K., and Katsura, T. (2017a). Synthesis and crystal structure of $LiNbO_3$-type $Mg_3Al_2Si_3O_{12}$: A possible indicator of shock conditions of meteorites. American Mineralogist: Journal of Earth and Planetary Materials, 102(9), 1947-1952.

Ishii, T., Tsujino, N., Arii, H., Fujino, K., Miyajima, N., Kojitani, H., Kunimoto, T., and Akaogi, M. (2017b). A shallow origin of so-called ultrahigh-pressure chromitites, based on single-crystal X-ray structure analysis of the high-pressure $Mg_2Cr_2O_5$ phase, with modified ludwigite-type structure. American Mineralogist: Journal of Earth and Planetary Materials, 102(10), 2113-2118.

Ishii, T., Yamazaki, D., Tsujino, N., Xu, F., Liu, Z., Kawazoe, T., . Yamamoto, T., Druzhbin, D., Wang, L., Higo, Y., Tange, Y., Yoshino, T., and Katsura, T. (2017c). Pressure generation to 65 GPa in a Kawai-type multi-anvil apparatus with tungsten carbide anvils. High Pressure Research, 37(4), 507-515.

Ishii, T., Huang, R., Fei, H., Koemets, I., Liu, Z., Maeda, F., Yuan, L., Wang, L., Druzhbin, D., Yamamoto, T., Bhat, S., Farla, R., Kawazoe, T., Tsujino, N., Kulik, E., Higo, Y., Tange, Y., and Katsura, T. (2018a). Complete agreement of the post-spinel transition with the 660-km seismic discontinuity. Scientific reports, 8(1), 1-6.

Ishii, T., Kojitani, H., and Akaogi, M. (2018b). Phase relations and mineral chemistry in pyrolitic mantle at 1600–2200° C under pressures up to the uppermost lower mantle: Phase transitions around the 660-km discontinuity and dynamics of upwelling hot plumes. Physics of the Earth and Planetary Interiors, 274, 127-137.

Ishii, T., Sakai, T., Kojitani, H., Mori, D., Inaguma, Y., Matsushita, Y., Yamaura, K., and Akaogi, M. (2018c). High-Pressure Phase Relations and Crystal Structures of Postspinel Phases in MgV_2O_4, FeV_2O_4, and $MnCr_2O_4$: Crystal Chemistry of AB_2O_4 Postspinel Compounds. Inorganic chemistry, 57, 6648-6657.

Ishii, T., Uenver-Thiele, L., Woodland, A. B., Alig, E., & Boffa Ballaran, T. (2018d). Synthesis and crystal structure of Mg-bearing Fe_9O_{11}: New insight in the complexity of Fe-Mg oxides at conditions of the deep upper mantle. American Mineralogist: Journal of Earth and Planetary Materials, 103(11), 1873-1876.

374 Ishii, T., Huang, R., Myhill, R., Fei, H., Koemets, I., Liu, Z., Maeda, F., Yuan, L., Wang, L.,
375 Druzhbin, D., Yamamoto, T., Bhat, S., Farla, R., Kawazoe, T., Tsujino, N., Kulik, E., Higo,
376 Y., Tange, Y., and Katsura, T. (2019a). Sharp 660-km discontinuity controlled by extremely
377 narrow binary post-spinel transition. Nature Geoscience, 12(10), 869-872.

378 Ishii, T., Liu, Z., and Katsura, T. (2019b). A Breakthrough in Pressure Generation by a Kawai-
379 Type Multi-Anvil Apparatus with Tungsten Carbide Anvils. Engineering, 5(3), 434-440.

380 Ishii, T., Kojitani, H., and Akaogi, M. (2019c). Phase relations of Harzburgite and MORB up
381 to the uppermost lower mantle conditions: Precise comparison with Pyrolite by multisample
382 cell high-pressure experiments with implication to dynamics of subducted slabs. Journal of
383 Geophysical Research: Solid Earth, 124, 3491-3507.

384 Ishii, T., Miyajima, N., Sinmyo, R., Kojitani, H., Mori, D., Inaguma, Y., and Akaogi, M. (2020).
385 Discovery of New Structured Post-Spinel $MgFe_2O_4$: Crystal Structure and High-Pressure
386 Phase Relations. Geophysical Research Letters, 47(6), e2020GL087490.

387 Ishii, T., Criniti, G., Bykova, E., Dubrovinsky, L., Katsura, T., Arii, H., Kojitani, H., and
388 Akaogi, M. (2021). High-pressure syntheses and crystal structure analyses of a new low-
389 density I_2O_4-related and $CaTi_2O_4$-type $MgAl_2O_4$ phases. American Mineralogist: Journal of
390 Earth and Planetary Materials, 106(7), 1105-1112.

391 Ishii, T., Ohtani, E., Shatskiy, A. (2022a) Aluminum and hydrogen partitioning between
392 bridgmanite and high-pressure hydrous phases: Implications for water storage in the lower
393 mantle. Earth and Planetary Science Letters, 583, 117441,.

394 Ishii, T., Miyajima, N., Criniti, G., Hu, Q., Glazyrin, K., and Katsura, T. High pressure-
395 temperature phase relations of basaltic crust up to mid-mantle conditions. Earth and
396 Planetary Science Letters, 584, 117472 (2022b).

Ito, E. Multi-anvil cells and high-pressure experimental methods. In: Schubert G, editor. Treatise on geophysics. 2nd ed., vol. 2, Amsterdam: Elsevier; 2015. p. 233–261.

Leinenweber, K., Utsumi, W., Tsuchida, Y., Yagi, T., and Kurita, K. (1991). Unquenchable high-pressure perovskite polymorphs of $MnSnO_3$ and $FeTiO_3$. Physics and Chemistry of Minerals, 18(4), 244-250.

Ismailova, L., Bykova, E., Bykov, M., Cerantola, V., McCammon, C., Ballaran, T.B., Bobrov, A., Sinmyo, R., Dubrovinskaia, N., Glazyrin, K., Liermann, H.P., Kupenko, I., Hanfland, M., Prescher, C., Prakapenka, V., Svitlyk, V., and Dubrovinsky, L. (2016). Stability of Fe, Al-bearing bridgmanite in the lower mantle and synthesis of pure Fe-bridgmanite. Science advances, 2(7), e1600427.

Kojitani, H., Katsura, T., and Akaogi, M. (2007). Aluminum substitution mechanisms in perovskite-type $MgSiO_3$: an investigation by Rietveld analysis. Physics and Chemistry of Minerals, 34(4), 257-267.

Kubo, A., and Akaogi, M. (2000). Post-garnet transitions in the system $Mg_4Si_4O_{12}$–$Mg_3Al_2Si_3O_{12}$ up to 28 GPa: phase relations of garnet, ilmenite and perovskite. Physics of the Earth and Planetary Interiors, 121(1-2), 85-102.

Lauterbach, S., McCammon, C. A., Van Aken, P., Langenhorst, F., and Seifert, F. (2000). Mössbauer and ELNES spectroscopy of (Mg, Fe)(Si, Al)O_3 perovskite: A highly oxidised component of the lower mantle. Contributions to Mineralogy and Petrology, 138(1), 17-26.

Liu Z., Ishii T., and Katsura T. (2017a). Rapid decrease of $MgAlO_{2.5}$ component in bridgmanite with pressure. Geochemical Perspective Letters, 5, 12-18.

Liu, Z., Nishi, M., Ishii, T., Fei, H., Miyajima, N., Ballaran, T. B., Ohfuji, H., Sakai, T., Wang, L., Shcheka, S., Arimoto, T., Tange, Y., Higo, Y., Irifune, T., and Katsura, T. (2017b). Phase

relations in the system $MgSiO_3$-Al_2O_3 up to 2300 K at lower mantle pressures. Journal of Geophysical Research: Solid Earth, 122(10), 7775-7788.

Liu, Z., McCammon, C., Wang, B., Dubrovinsky, L., Ishii, T., Bondar, D., Nakajima, A., Tange, Y., Higo, Y., Cui, T., Liu, B., and Katsura, T. (2020) Stability and solubility of the $FeAlO_3$ component in bridgmanite at uppermost lower mantle conditions. Journal of Geophysical Research: Solid Earth, 125(2).

McCammon, C. A., Chaskar, V., and Richards, G. G. (1991). A technique for spatially resolved Mossbauer spectroscopy applied to quenched metallurgical slags. Measurement Science and Technology, 2(7), 657.

McCammon, C. A. (1994). A Mössbauer milliprobe: Practical considerations. Hyperfine Interactions, 92(1), 1235-1239.

McCammon, C., Hutchison, M., and Harris, J. (1997). Ferric iron content of mineral inclusions in diamonds from Sao Luiz: A view into the lower mantle. Science, 278(5337), 434-436.

McCammon, C. A., Lauterbach, S., Seifert, F., Langenhorst, F., & Van Aken, P. A. (2004). Iron oxidation state in lower mantle mineral assemblages: I. Empirical relations derived from high-pressure experiments. Earth and Planetary Science Letters, 222, 435-449.

Navrotsky, A. (1999). A lesson from ceramics. Science, 284, 1788–1789.

Navrotsky, A., Schoenitz, M., Kojitani, H., Xu, H., Zhang, J., Weidner, D. J., & Jeanloz, R. (2003). Aluminum in magnesium silicate perovskite: Formation, structure, and energetics of magnesium-rich defect solid solutions. Journal of Geophysical Research: Solid Earth, 108(B7).

Ono, S., Ito, E., and Katsura, T. (2001). Mineralogy of subducted basaltic crust (MORB) from 25 to 37 GPa, and chemical heterogeneity of the lower mantle. Earth and Planetary Science Letters, 190, 57-63.

444 Prescher, C., McCammon, C., and Dubrovinsky, L. (2012). MossA: a program for analyzing
445 energy-domain Mössbauer spectra from conventional and synchrotron sources. Journal of
446 Applied Crystallography, 45(2), 329-331.

447 Reali, R., Van Orman, J. A., Pigott, J. S., Jackson, J. M., Boioli, F., Carrez, P., and Cordier, P.
448 (2019). The role of diffusion-driven pure climb creep on the rheology of bridgmanite under
449 lower mantle conditions. Scientific reports, 9(1), 1-9.

450 Uenver-Thiele, L., Woodland, A. B., Miyajima, N., Ballaran, T. B., and Frost, D. J. (2018).
451 Behaviour of Fe_4O_5–$Mg_2Fe_2O_5$ solid solutions and their relation to coexisting Mg–Fe
452 silicates and oxide phases. Contributions to Mineralogy and Petrology, 173(3), 1-16.

453 White, R. S., and McKenzie, D. (1995). Mantle plumes and flood basalts. Journal of
454 Geophysical Research: Solid Earth, 100(B9), 17543-17585.

455 Yoshino, T., Kamada, S., Zhao, C., Ohtani, E., and Hirao, N. (2016). Electrical conductivity
456 model of Al-bearing bridgmanite with implications for the electrical structure of the Earth's
457 lower mantle. Earth and Planetary Science Letters, 434, 208-219.

458 **Figure Captions**

459 **Figure 1.** Room-temperature Mössbauer spectrum of the recovered sample synthesized at 27
460 GPa and 2000 K. The red shaded area is assigned to non-magnetic Fe^{3+}. The grey shaded area
461 is assigned to weakly magnetic Fe^{3+}. Spectra of samples quenched from 1700 K and 2300 K
462 contain only non-magnetic Fe^{3+}.

463 **Figure 2.** X-ray diffraction pattern of the recovered sample synthesized at 27 GPa and 2000 K.
464 Stars indicate possible peaks of $(Mg,Al,Fe^{3+})O_4$ post-spinel phase (see text). LN, lithium
465 niobate phase.

466 **Figure 3.** Back-scattered electron images of recovered samples at 27 GPa and 1700-2300 K.
467 White grains are platinum from the platinum capsule when polishing. LN, lithium niobate
468 phase; Crn, corundum; PS, $(Mg,Al,Fe^{3+})O_4$ post-spinel phase.

469 **Figure 4.** Solubility of $MgSiO_3$, $FeAlO_3$, Fe_2O_3 $Fe_{2/3}SiO_3$, and $MgFeO_{2.5}$ components in the
470 perovskite-structured phase at 27 GPa as a function of temperature.

Table 1. Experimental conditions, phase assemblages, and chemical compositions of recovered bridgmanite.

Run No.	I-1003	I-969	I-991
Temperature (K)	1700	2000	2300
Heating duration (h)	20	13	2
Phases	LN+Crn+PS	LN+Crn+PS	LN+Crn+PS
n	8	9	12
Composition (wt.%)			
MgO	9.44(37)	9.95(30)	10.91(38)
SiO_2	14.74(62)	15.62(50)	15.59(47)
Al_2O_3	29.05(58)	28.40(35)	27.18(61)
Fe_2O_3	47.61(82)	46.32(65)	45.21(73)
Total	100.85(130)	100.26(122)	98.89(148)
Composition (pfu) (O = 3)			
Mg	0.284(9)	0.300(6)	0.333(9)
Si	0.298(14)	0.315(8)	0.319(6)
Al	0.691(6)	0.676(5)	0.656(9)
Fe	0.723(8)	0.704(10)	0.697(12)
Cation total	1.996(7)	1.995(3)	2.005(4)
Mole fraction			
$MgSiO_3$	28(1)	30(1)	32(1)
$FeAlO_3$	69(1)	68(1)	65(1)
Fe_2O_3	1.2(9)	0.9(11)	1.3(18)
$Fe^{3+}_{2/3}SiO_3$	1.4(1.7)	1.6(10)	N
$MgFeO_{2.5}$	N	N	1.4(11)
$Fe^{3+}/\Sigma Fe$	100(5)	100(3)	100(5)
Hyperfine parameters			
CS for Fe^{3+}	0.33(1)	0.319(5)[a]	0.32(1)
QS for Fe^{3+}	0.92(2)	0.895(5)	0.92(2)
FWHM	0.48(4)	0.36(2)	0.47(4)

Abbreviations: LN, $LiNbO_3$-type phase; Crn, corundum; PS, $A^{2+}B^{3+}{}_2O_4$ post-spinel phase; N, not observed; *n*, number of analyzed points; CS, center shift relative to α-Fe (mm/s); QS, quadrupole splitting (mm/s); FWHM, full width at half maximum (mm/s).

Numbers in parentheses for chemical composition data indicate one standard deviations of the mean in the analyses.

[a]Broad, weak magnetic Fe^{3+} component with CS = 0.1(1) mm/s was also observed in the fitting (see Fig. 1).

Mole fractions of each component were calculated as follows (also see the text):

1. All Al is combined with corresponding amount of Fe^{3+} to form the $FeAlO_3$ component.

2. The A-site vacancy, corresponding to 1/3 of the A-site, is used to allocate Fe and Si to the $Fe^{3+}_{2/3}SiO_3$ component

3. The O-vacancy corresponding to 0.5 of the $MgFe_{3+}O_{2.5}$ component forms the basis for the allocation of Fe and Mg.

4. The rest of Fe is allocated to the Fe_2O_3 component.

5. The rest of Mg and Si is allocated to the $MgSiO_3$ component.

This is the peer-reviewed, final accepted version for American Mineralogist, published by the Mineralogical Society of America.
The published version is subject to change. Cite as Authors (Year) Title. American Mineralogist, in press.
DOI: https://doi.org/10.2138/am-2022-8457. http://www.minsocam.org/

488 **Table 2.** Chemical compositions of recovered post-spinel phases and corundum.

Post-spinel phase, I-1003 (27 GPa, 1700 K), *n* = 9					
Oxide wt.%	MgO	SiO_2	Al_2O_3	Fe_2O_3	Total
	21.32(31)	0.86(22)	29.93(52)	45.69(35)	97.81(46)
Cation number (O=4)	Mg	Si	Al	Fe^{3+}	Total
	0.921(13)	0.025(6)	1.022(15)	0.996(10)	2.965(5)
Post-spinel phase, I-969 (27 GPa, 2000 K) , *n* = 8					
Oxide wt.%	MgO	SiO_2	Al_2O_3	Fe_2O_3	Total
	22.73(38)	0.75(4)	30.39(60)	45.05(48)	98.93(73)
Cation number (O=4)	Mg	Si	Al	Fe^{3+}	Cation
	0.968(9)	0.022(1)	1.024(14)	0.969(15)	2.982(3)
Corundum, I-969 (27 GPa, 2000 K), *n*= 6					
Oxide wt.%	MgO	SiO_2	Al_2O_3	Fe_2O_3	Total
	4.20(10)	6.19(27)	73.84(56)	14.80(56)	99.03(65)
Cation number (O=3)	Mg	Si	Al	Fe^{3+}	Cation
	0.113(3)	0.112(5)	1.574(12)	0.201(7)	2.000(1)
Post-spinel phase, I-991 (27 GPa, 2300 K), *n* = 8					
Oxide wt.%	MgO	SiO_2	Al_2O_3	Fe_2O_3	Total
	21.19(18)	1.64(9)	30.44(41)	44.48(41)	97.75(55)
Cation number (O=4)	Mg	Si	Al	Fe^{3+}	Cation
	0.910(1)	0.047(2)	1.033(11)	0.964(5)	2.954(3)
Corundum, I-991 (27 GPa, 2300 K) , *n* = 6					
Oxide wt.%	MgO	SiO_2	Al_2O_3	Fe_2O_3	Total
	3.73(4)	5.24(17)	74.27(77)	14.49(32)	97.72(92)
Cation number (O=3)	Mg	Si	Al	Fe^{3+}	Cation
	0.102(1)	0.096(3)	1.604(4)	0.200(3)	2.002(1)

489 *n*, number of analyzed points. Numbers in parentheses indicate one standard deviations of the
490 mean in the analyses.

Acknowledgements

We thank H. Fischer and R. Njul for the preparation of cell assemblies and thin-section samples for Mössbauer measurements, respectively. We are also grateful to Prof. R.G. Tronnes and Prof. O. Müntener for their constructive comments. We also thank two anonymous reviewers for their fruitful comments. This work was funded by research projects approved by the European Research Council (ERC) under the European Union's Horizon 2020 research and innovation programme (Proposal No. 787 527) to T. Katsura and the German Research Foundation (DFG) grant (IS350/1-1) to T. Ishii.

Fig. 1

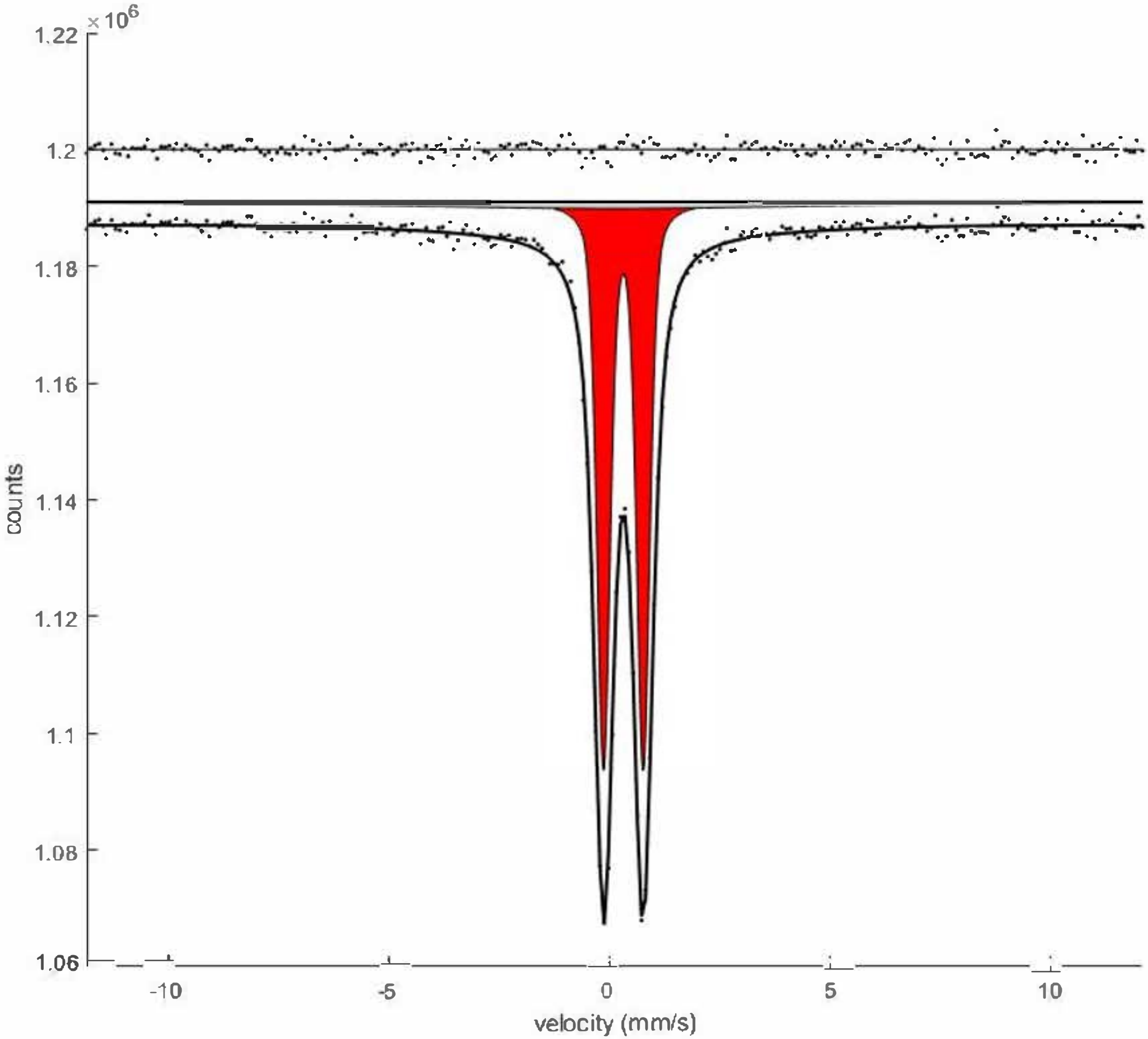
× 10^6
1.22
1.2
1.18
1.16
1.14
1.12
1.1
1.08
1.06
counts
-10
-5
0
5
10
velocity (mm/s)

Fig. 2

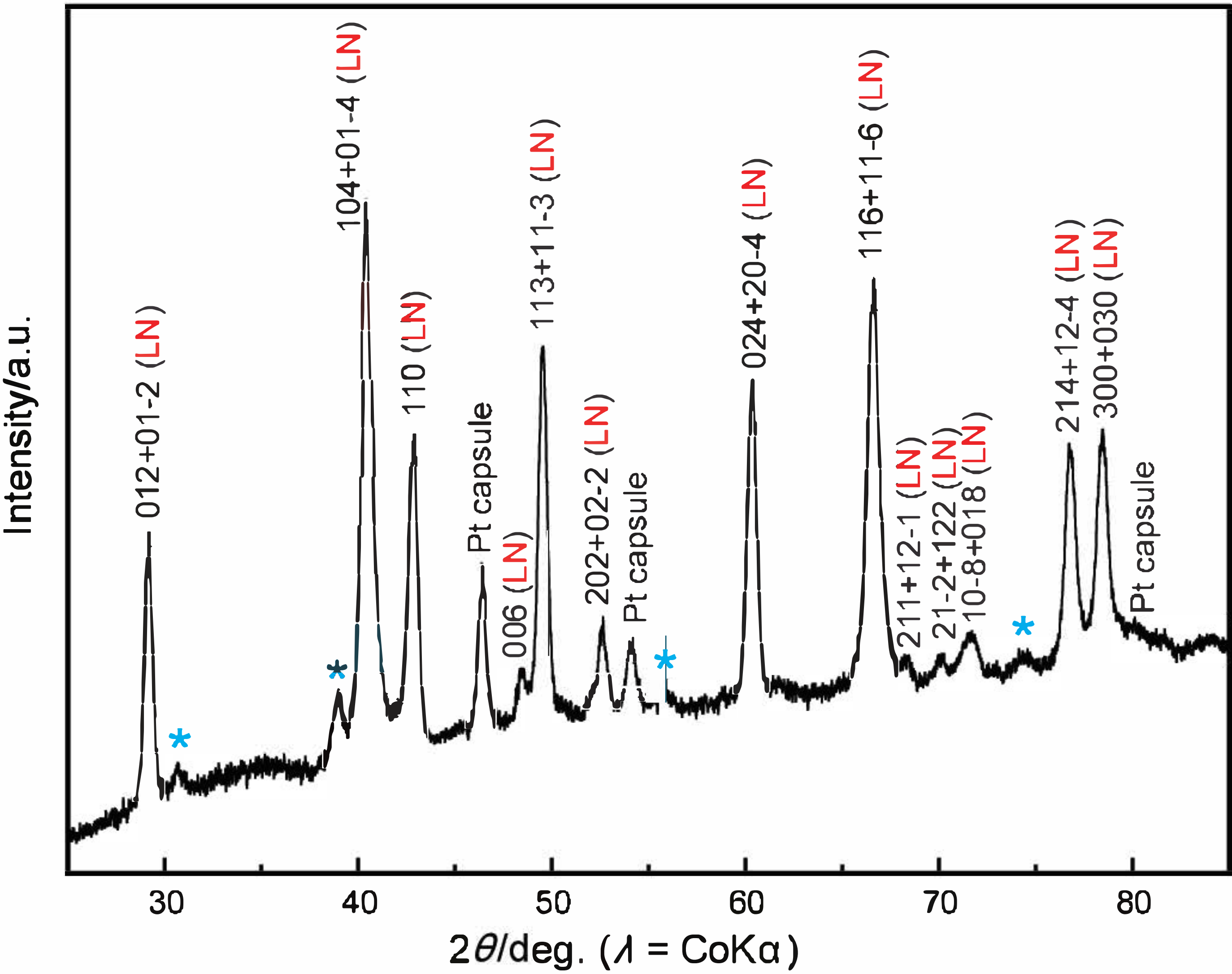
Intensity/a.u.
012+01-2 (LN)
104+01-4 (LN)
110 (LN)
Pt capsule
113+11-3 (LN)
006 (LN)
202+02-2 (LN)
Pt capsule
024+20-4 (LN)
116+11-6 (LN)
211+12-1 (LN)
21-2+122 (LN)
10-8+018 (LN)
214+12-4 (LN)
300+030 (LN)
Pt capsule
*
30
40
50
60
70
80
2θ/deg. (λ = CoKα)

Fig. 3

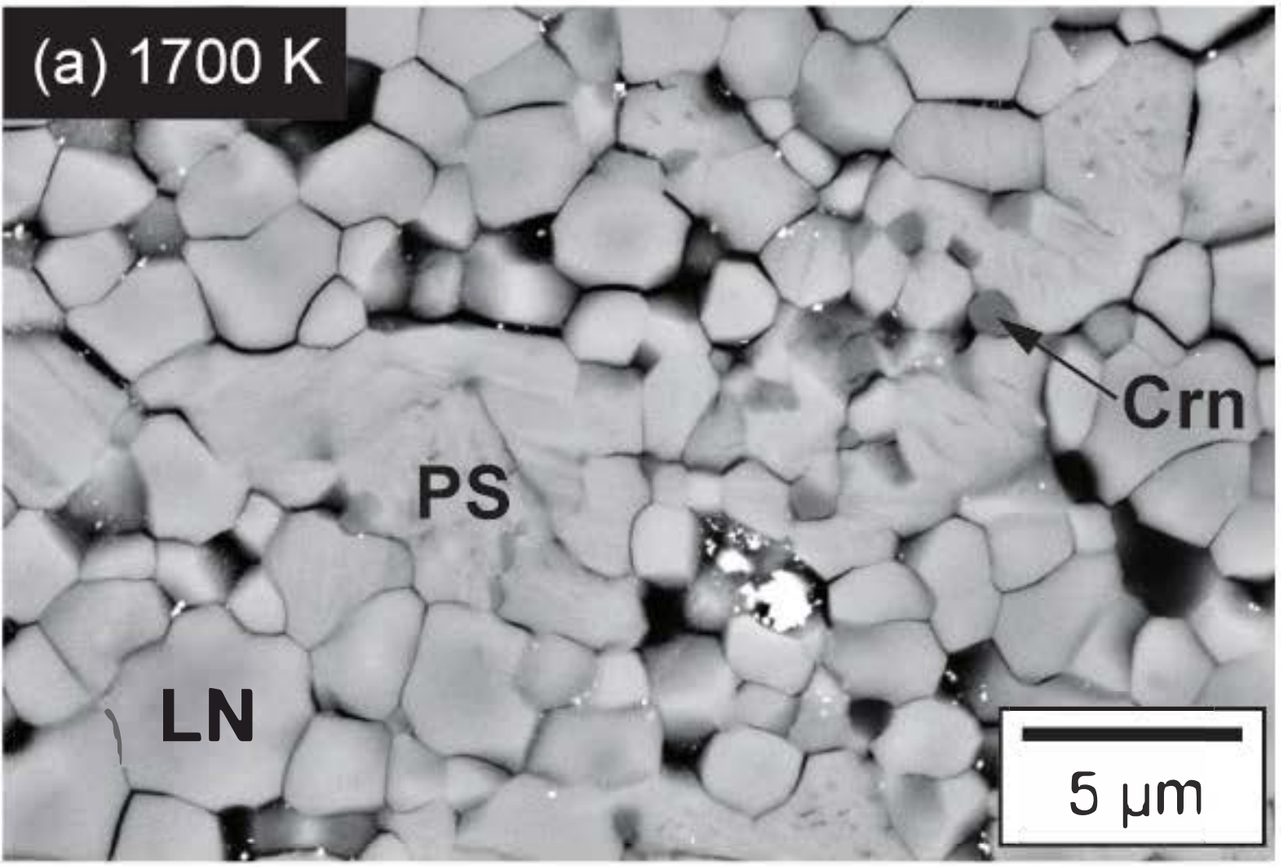
(a) 1700 K
Crn
PS
LN
5 μm

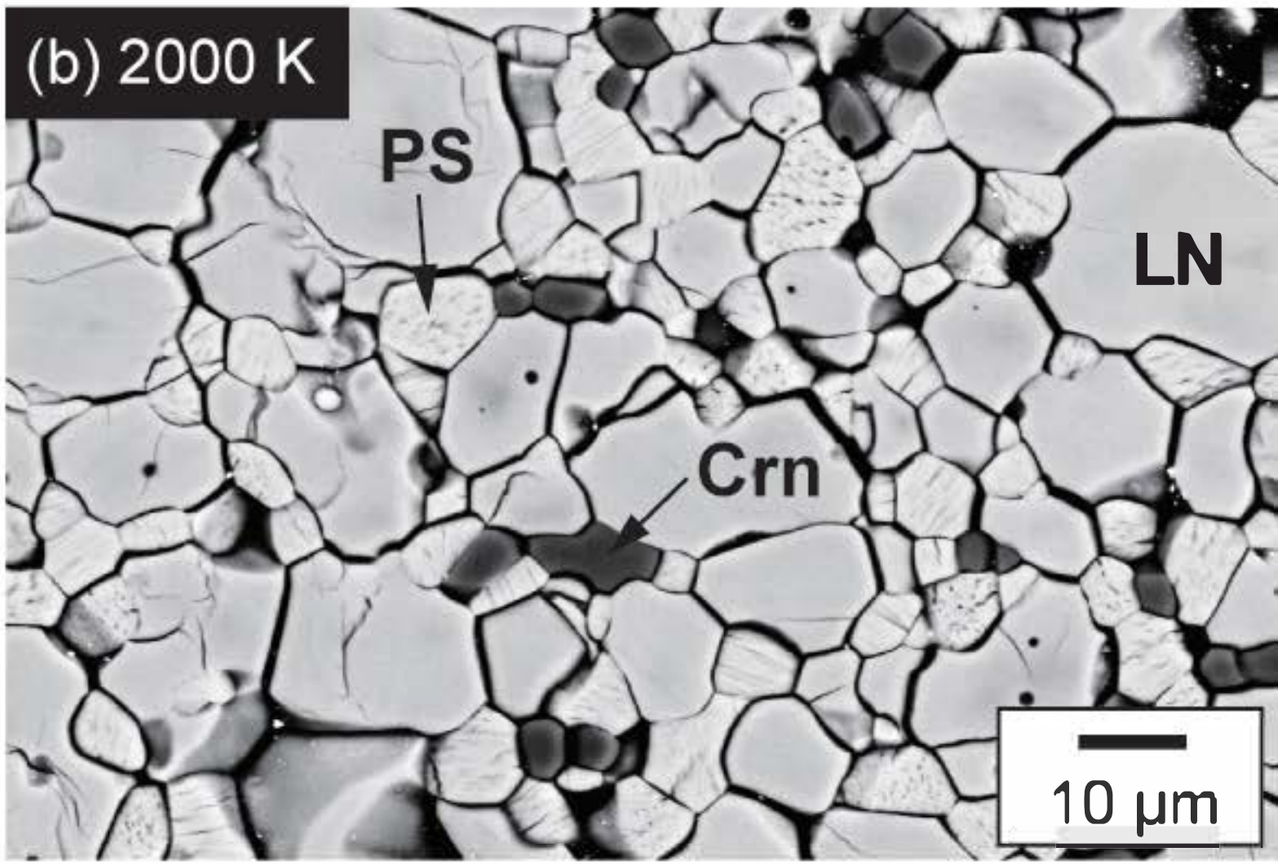
(b) 2000 K
PS
LN
Crn
10 μm

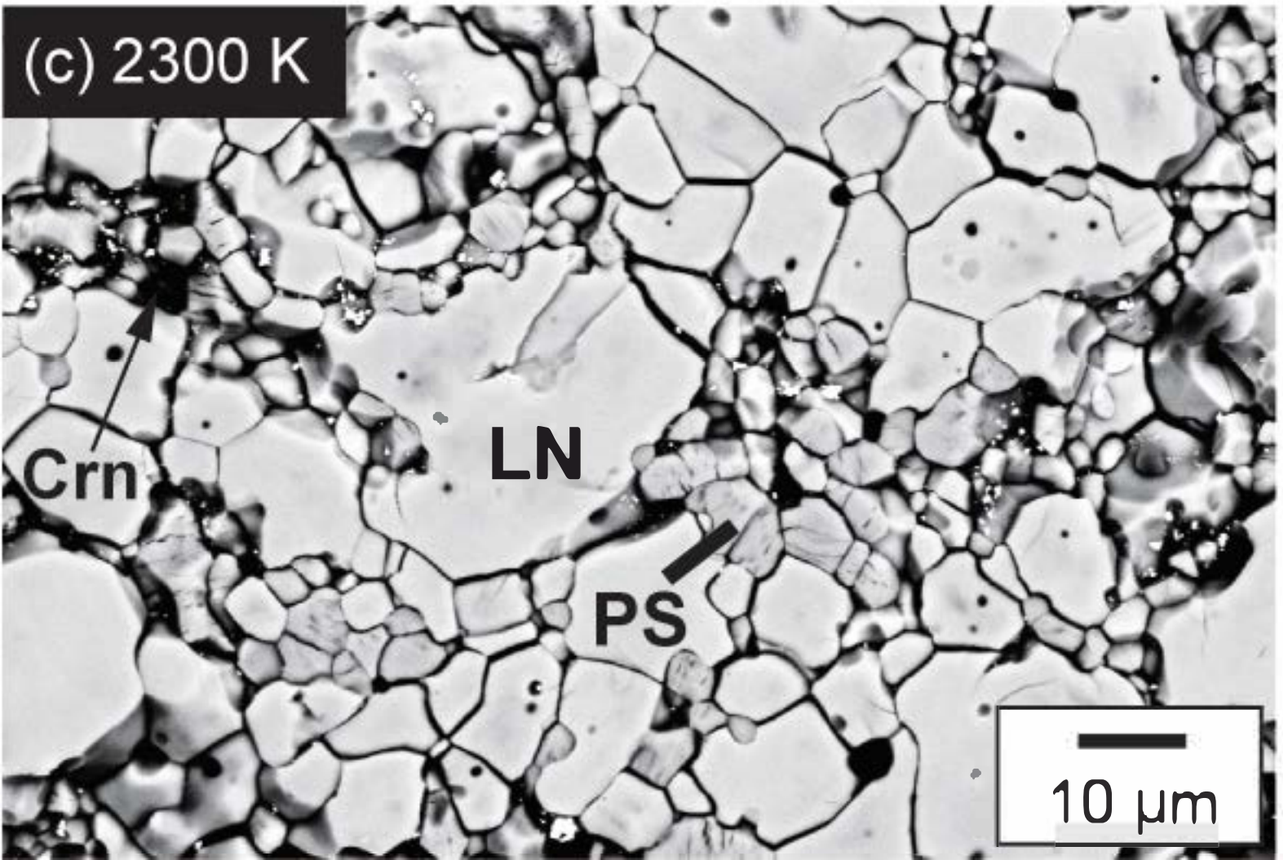
(c) 2300 K
Crn
LN
PS
10 μm

Fig. 4

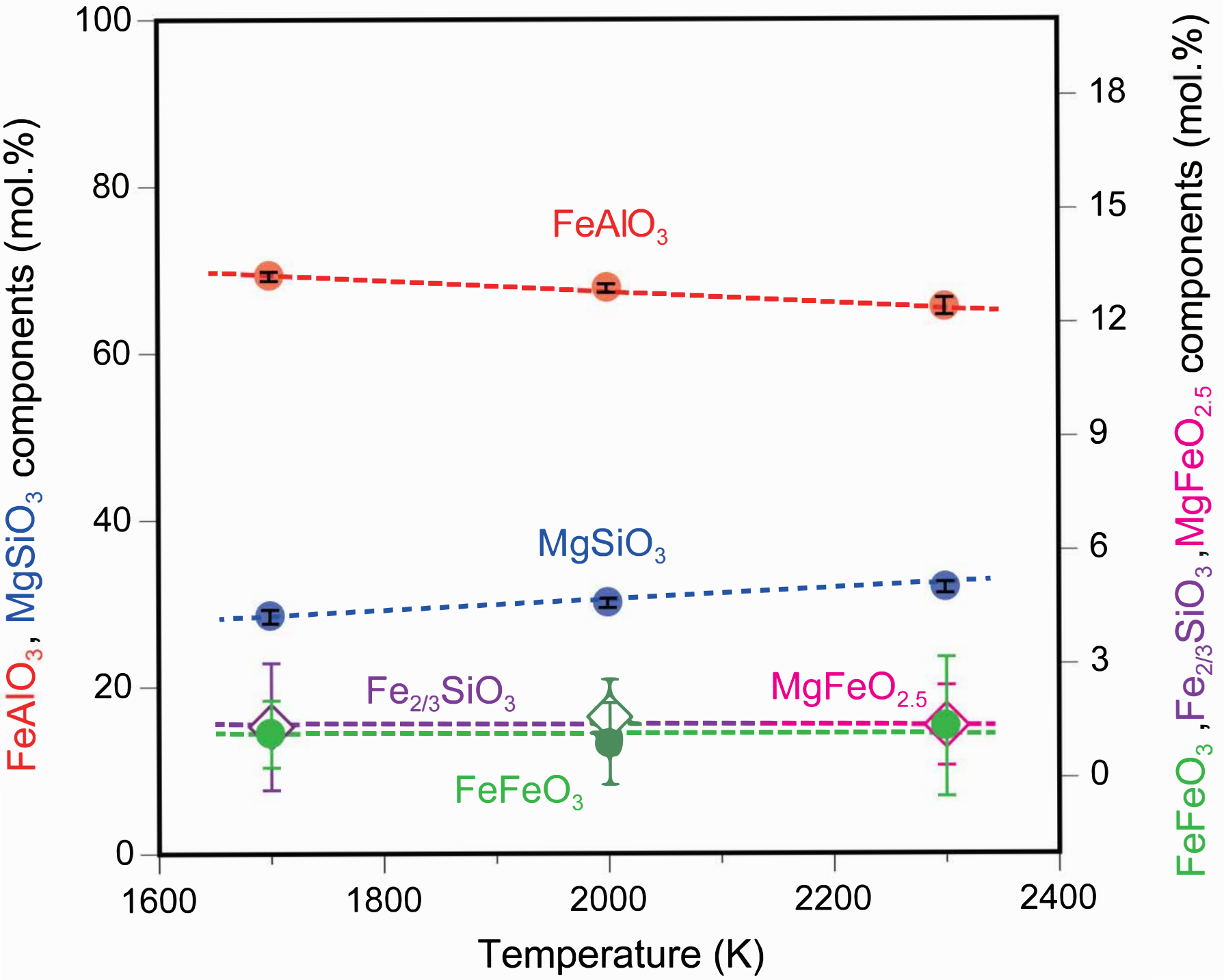
100
80
60
40
20
0
18
15
12
9
6
3
0
1600
1800
2000
2200
2400
Temperature (K)
FeAlO3, MgSiO3 components (mol.%)
FeFeO3 ,Fe2/3SiO3 ,MgFeO2.5 components (mol.%)
FeAlO3
MgSiO3
Fe2/3SiO3
MgFeO2.5
FeFeO3